Available online at www.sciencedirect.com
SCIENCE DIRECT®
European Journal of Pharmaceutics and Biopharmaceutics 64 (2006) 38–50
European Journal of Pharmaceutics and Biopharmaceutics
www.elsevier.com/locate/ejpb

Research paper

Quantitative measurements of localized density variations in cylindrical tablets using X-ray microtomography

Virginie Busignies [a], Bernard Leclerc [a], Patrice Porion [b], Pierre Evesque [c], Guy Couarraze [a], Pierre Tchoreloff [a,*]

[a] Centre d'études Pharmaceutiques de l'Université Paris XI, Innovation Thérapeutique: du Fondamental au Médicament, Châtenay-Malabry, France
[b] Centre de Recherche sur la Matière Divisée – UMR 6619, CNRS and Université d'Orléans, Orléans, France
[c] Laboratoire de Mécanique: Sols – Structure – Matériaux – UMR 8579, Ecole centrale de Paris, Châtenay-Malabry, France

Received 5 October 2005; accepted in revised form 17 February 2006
Available online 18 April 2006

Abstract

Direct compaction is a complex process that results in a density distribution inside the tablets which is often heterogeneous. Therefore, the density variations may affect the compact properties. A quantitative analysis of this phenomenon is still lacking. Recently, X-ray microtomography has been successfully used in pharmaceutical development to study qualitatively the impact of tablet shape and break-line in the density of pharmaceutical tablets. In this study, we evaluate the density profile in microcrystalline cellulose (Vivapur 12®) compacts obtained at different mean porosity (ranging from 7.7% to 33.5%) using X-ray tomography technique. First, the validity of the Beer–Lambert law is studied. Then, density calibration is performed and density maps of cylindrical tablets are obtained and visualized using a process with colour-scale calibration plot which is explained. As expected, important heterogeneity in density is observed and quantified. The higher densities in peripheral region were particularly investigated and appraised in regard to the lower densities observed in the middle of the tablet. The results also underlined that in the case of pharmaceutical tablets, it is important to differentiate the mechanical properties representative of the total volume tablet and the mechanical properties that only characterize the tablet surface like the Brinell hardness measurements.

Keywords: X-ray tomography; Compaction; Tablet; Density distribution; Anisotropy; Quantitative analysis; 3D imaging; Mechanical properties

1. Introduction

Direct compaction is commonly used in pharmaceutical industry to produce pharmaceutical tablets. The density distribution inside the tablets is often heterogeneous due to interparticle frictions and die wall frictions [1]. At the beginning of the compaction, interparticle frictions are predominant, but the die wall frictions become more important when the pressures are increased. More, the shape of tablets used in pharmaceutical industry differs from flat-face cylindrical tablet to more complex geometries with various embossing. The consequence is that the density variations in pharmaceutical tablets may be important and affect the compact mechanical properties. Train [1] performed the first study on the density variation in powder compacts. Later, density distribution was investigated using NMR tomography [2] or autoradiography [3]. Sinka et al. [4] also used surface hardness tests on tablets' cross-section. Recently, X-ray microtomography has been successfully used in pharmaceutical development. Farber et al. [5] used this method to study the porosity and the morphology of pharmaceutical granules. Sinka et al. [6] have shown the dependence of tablet shape and break-line on the density variations of pharmaceutical tablets.

The X-ray tomography which allows 3D characterization of micro-structure has some advantages compared to other methods [7]. This is a nondestructive investigation

* Corresponding author. Laboratoire de Physique Pharmaceutique, Centre d'études Pharmaceutiques de l'Université Paris XI, 5 Rue Jean Baptiste Clément, 92296 Châtenay-Malabry Cedex, France. Tel.: +33 1 46 83 56 11; fax: +33 1 46 83 58 82.
E-mail addresses: pierre.tchoreloff@phypha.u-psud.fr, pierre.tchoreloff@cep.u-psud.fr (P. Tchoreloff).

0939-6411/$ - see front matter © 2006 Elsevier B.V. All rights reserved.
doi:10.1016/j.ejpb.2006.02.007

from which many 2D sections can be extracted and contrary to 2D observations, there are no artefacts due to sample preparation. More, the micro-structural characterization is possible at high and medium resolution (from 1 to few hundred microns). Nevertheless, as the sample should rotate in the field of view of the detector, a compromise must be found between the maximum sample size and the spatial resolution. One other disadvantage could be the time for a complete scan. It is strongly influenced by the resolution, the size of the sample, the resolution of the CCD camera and the spot size of the X-ray source. For tableting, X-ray tomography is more adapted to the analysis of density variations than the use of surface hardness that is a destructive technique which requires careful specimen preparation. More, the resolution is limited by the spacing between indentations [6].

In this work, we try to evaluate quantitatively the density variation in cylindrical compacts of microcrystalline cellulose using the X-ray microtomography. Beforehand, perfecting of the technique is achieved with the demonstration of the validity of the Beer–Lambert law and the construction of a colour-scale calibration plot of density. Then, the density maps are obtained for different tablets and they are discussed.

2. X-ray microtomography principle and its limits

The X-ray microfocus computed tomography (X-ray μCT) method is a nondestructive inspection technique which provides cross-sectional images in different planes from the sample [8]. The principle of the third generation CT imaging is illustrated in Fig. 1. The sample is placed on a precision turntable in a divergent beam of X-rays. A detector (which is in fact a one-dimension or two-dimension array of detectors) is used to measure the local intensity distribution of a diverging X-ray beam transmitted through the sample, as the sample is rotated step-by-step angle in the beam, around its axis. The sample position from the X-ray source determines the geometrical magnification (i.e. the resolution which is also limited by the detector size) according to the principle of the cone-beam geometry. This leads to a series of radiographs also called projection images at different viewing angles. From this set, one can reconstruct a three-dimensional representation of the structure and/or a composition distribution within a sample, using a mathematical algorithm based on the Beer–Lambert law of absorption (see Eq. (1)). This reconstruction is called a tomogram; it has a spatial volume resolution, which is called a voxel. To facilitate the analysis, the tomogram can be decomposed in a series of cross-sectional images in a chosen plane, and these cuts can be interpreted in terms of density or composition distribution after the calibration process. According to the Beer–Lambert law, the dependence of the intensity $I(x)$ of the X-ray beam after its crossing through a layer of homogeneous material of thickness x is related to the initial intensity I_0 and the linear attenuation coefficient μ through

$$I(x) = I = I_0 \, e^{-\mu x} \quad \text{or} \quad -\ln(I/I_0) = \mu x, \tag{1}$$

where μ is a local coefficient which characterizes the material; it is expected to depend on the chemical nature of the compounds and to vary linearly with each local amount of compound [9,10] according to Eqs. (2) and (3)

$$\mu = \rho_i(\mu_{i0}/\rho_{i0}), \tag{2}$$

where ρ_i is the real local density of chemical i, and μ_{i0}/ρ_{i0} is the ratio of its normal absorption coefficient to its normal density ρ_{i0} (in g cm^{-3}). When few chemical compounds are mixed one uses the additivity property of local absorption coefficient and writes

$$\mu = \sum_i \rho_i(\mu_{i0}/\rho_{i0}) \tag{3}$$

leading to the generalised Beer–Lambert law for monochromatic X-ray beam

$$\ln(I/I_0) = -\int \mu(l)\,\mathrm{d}l, \tag{4}$$

where $\mathrm{d}l$ is the infinitesimal length along the trajectory of X-ray beam in the material, and the summation runs over the whole path. Neglecting refraction effect from local heterogeneities, one can use the linearity of Eq. (4) to reconstruct the density distribution by inversion of the set of Eq. (4) obtained at different angles.

Things become more intricate when X-ray beam is non-monochromatic, since it is known that the μ_{i0} coefficients depend on X-ray wavelength λ and because a sum of exponentials is not an exponential. Indeed, imagine that a lower energy X-ray beam is more strongly absorbed than a higher energy one, and that the initial beam is composed of these two wavelengths, then the energy distribution spectrum of the beam changes as it passes through the sample and the beam becomes harder, this effect is called "beam hardening". Consequently for polychromatic X-ray source, the attenuation of a homogeneous sample is not always strictly proportional to its thickness. In other words, the Beer–Lambert law is not valid any more. As, the projection data are not linear with the sample thickness, the reconstruction

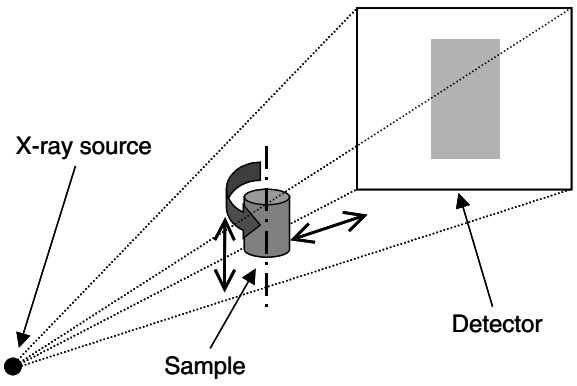

Fig. 1. X-ray microtomography principle.

produces some distortions, such as pronounced edges or false density gradients. This artefact which is the most important for a quantitative density measurement can be corrected by mathematical method during the reconstruction of the tomogram or by the introduction of an adequate filter to pre-filter the X-ray beam.

In addition, the X-ray tomography technique generates other artefacts. The most common one is the "ring artefacts" which is due to the sample rotation [8]. This artefact can be partially corrected using mathematically algorithm during the reconstruction process. Some other correction artefacts come from irregularities of the X-ray tube emission and of the CCD camera sensitivity map [6,10]. They can be partly avoided using the "flat-field" correction technique, which consists in calibrating the set-up from the acquisition of two empty field images (i.e. without sample), one with the X-ray source "on" and the other one with the source "off".

3. Materials and methods

3.1. Materials

The material used in this study is a microcrystalline cellulose (Vivapur 12®, 5601210932, JRS, Germany). A granular fraction between 100 and 180 μm was obtained by sieving on a mechanical sieve shaker (AS 200 digit®, Retsch, Germany) and was stored at 50% of relative humidity for at least 3 days. The fraction was mixed with 0.5% w/w of magnesium stearate (NF-BP-MF2 039445, Akcros Chemicals v.o.f., Netherlands) in a Turbula® mixer at 50 rpm for 5 min (type T2C, Willy A. Bachofen, Basel, Switzerland). The apparent particle density of the Vivapur 12® in a magnesium stearate mixture measured by helium pycnometry technique (Accupyc 1330, Micromeritics, Norcross, GA, USA) was 1.5380 ± 0.0007 g cm^{-3}.

3.2. Formation of compacts

Cylindrical compacts were obtained under compaction pressures range between about 40 and 280 MPa, using an eccentric Frogerais OA® tabletting press (Frogerais OA, Vitry-sur-Seine, France) [11]. The initial volume of the die was kept constant (1 cm^3, section of 1 cm^2 and height of 1 cm). Three days after compaction, the mean porosity ε of the tablets was calculated from the section, the height and the weight of the compacts knowing the particular density of the microcrystalline cellulose Vivapur 12® ($\rho_{part} = 1.538$ g cm^{-3}).

3.3. Brinell hardness measurements on cylindrical tablets

The Brinell hardness (called H_b in this work and expressed in MPa) was obtained using a microindentation test [12]. A stress was applied on the top side of the tablet by a spherical indentor with a 2.38 mm diameter at a rate of 0.06 mm min^{-1}. The maximal displacement of the indentor was 0.1 mm and the relaxation time was 5 min. The Brinell hardness (H_b) was calculated by the following equation:

$$H_b = \frac{2F}{\pi D(D - \sqrt{D^2 - d^2})}, \quad (5)$$

where F is the maximal load applied, D is the indentor diameter and d is the diameter of the indentation surface.

3.4. X-ray microtomography

Tomography experiments were carried out on a high resolution SkyScan-1072 XRCT® (SkyScan, Aartselaar, Belgium). This machine is equipped with an 80 kV X-ray micro-focus source (20–80 kV and 0–100 μA) with a spot size of 8 μm in diameter to illuminate the object with a divergent X-ray beam. Magnified transmitted projection pictures were detected by a two-dimensional X-ray CCD-camera with 1024×1024 pixels resolution 12-bit dynamic range sensor (fibre optic coupling, 3.7:1 image reduction). The SkyScan micro-CT used the Feldkamp cone-beam algorithm reconstruction method to take into account the conical geometry of the X-ray source [13].

For all the cylindrical tablets, the scanning parameters were as follows: the X-ray source was operated at a voltage U of 39.7 kV and a current I of 100 μA (i.e. $P = 4$ W) with an exposure time of 3.472 s per projection. Owing to the cone beam technique, 2D absorption data were taken at a size-magnification of 20× which led to a resolution of 15.63 μm per sensor pixel, leading to a 15.63 μm resolution size in the three directions after image reconstruction. To reduce the beam hardening artefacts, a 1 mm aluminium thick plate was placed over the X-ray source to filter the low energy X-rays. Complete acquisition of the whole sets of projection data was obtained after taking 414 projection images at different angles which were equally spaced ($\Delta\theta = 0.45°$) and which cover a range lightly superior to 180°. Then the sample is reconstructed through a set of about 900 cross-sectional images (1024×1024 pixels, 8-bit, BMP format) with a spatial resolution of 15.63 μm; and this reconstruction used the cone-beam reconstruction method (Skyscan software) with the option "Ring artefacts reduction" in addition, to reduce the ring artefact.

In this work, a set of 13 cylindrical tablets were studied. The characteristics of the cylindrical compacts are reported in Table 1. To reduce the acquisition time of the projection data, three samples, noted A, B and C, were built up as a superposition of 4 (samples A and B) or 5 (sample C) different cylindrical tablets. Fig. 2 reports the configuration of tablets inside each three samples. Each tablet has its axis parallel to the picture plane.

3.5. Image processing

X-ray tomography technique allows complete reconstruction of a three-dimensional object leading to a series

Table 1
Characteristics of the tablets

Tablet	Sample	Compaction pressure (MPa)	Porosity, ε (%)[a]	Mean apparent density ρ_{app} (g cm^{-3})[a]	I_0 mean (grey value)	I_{Min} (grey value)
1	C	282	7.67	1.420	62738	27284
2	C	219	8.34	1.410	62430	27394
3	C	199	9.72	1.388	62010	27498
4	C	180	11.81	1.356	62361	27670
5	C	162	12.43	1.347	61736	28199
6	B	157	12.54	1.345	61823	28420
7	B	138	14.89	1.309	61796	28802
8	B	124	15.14	1.305	61912	28851
9	A	106	16.33	1.287	62490	29433
10	B	108	17.06	1.275	61465	29266
11	A	80	21.32	1.210	62200	30450
12	A	59	26.83	1.125	62372	31836
13	A	40	33.51	1.023	62299	33882

Apparent density ρ_{app} and porosity ε are measured from the weight and volume of each tablet, knowing the particular density of microcrystalline cellulose Vivapur 12®. The intensities I_0 and I_{Min} are the mean values obtained from the analysis of 101 profiles for each tablet corresponding to the given apparent density. For example, this procedure is explained in Fig. 3 for the Tablet n°10.

[a] $\rho_{app} = (1 - \varepsilon)\ \rho_{part}$ with $\rho_{part} = 1.5380$ g cm^{-3}.

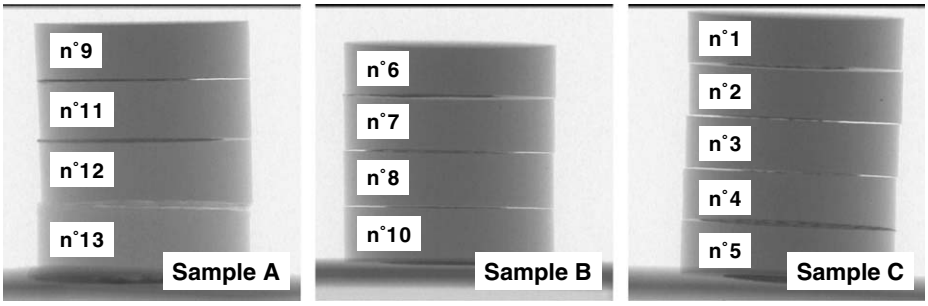

Fig. 2. Examples of projection image obtained for the 3 different samples A, B and C.

of cross-sectional images. In this paper, all these images were analysed using the ImageJ software which is a public domain Java image processing program [14]. The different image processing used in this study will be explained in all detail in the next sections.

4. Results and discussion

4.1. Validity of the Beer–Lambert law on projection images

Quantitative analysis of the density distribution inside the tablets requires the validity of the Beer–Lambert law, which states that the X-ray attenuation $-\ln(I/I_0)$ is linearly proportional to the density ρ of the material or/and to its thickness x (see Eq. (1)). Unfortunately, effects of ''nonlinearity'' were often observed on the X-ray attenuation due to the ''beam hardening'' artefact discussed in Section 2. As a result, the outer surface of the sample usually looks denser than it really is, whereas the central part looks lighter. So, this artefact affects the quantitative measurements of the density parameter. When it is present, this artefact can be removed by direct mathematical correction of the projection images before the reconstruction process. To check the validity of the Beer–Lambert law on the tablets under our experimental protocol, two different analyses were done from the projection images. Firstly, we studied the X-ray attenuation as a function of the apparent density ρ_{app} (at a given thickness x) using specific tablets; secondly, the attenuation was measured as a function of the thickness (at a known density).

In the first technique, for each tablet, one extracts from the projection images the zones of maximum and minimum transmitted intensities, that correspond to zones: (i) without material and (ii) with the material at its maximum thickness (see Fig. 3, for example); this allows for each tablet to determine the intensity of the nonattenuated X-ray beam I_0 (which correspond to the mean of the maximum values I_{Max}) and the intensity I_{Min} of the most attenuated signal; I_{Min} is obtained when the thickness of the matter is the larger, one gets $I_{Min} = I(d_0)$ according to the geometry of the experimental set-up, with d_0 being the cylindrical tablet diameter. As all tablets have closely similar diameters ($d_0 = 11.28$ mm), the attenuation curve can be obtained as a function of the apparent density by analysing the projection images of the 13 different tablets. Results are reported in Table 2 and Fig. 4. They show that the logarithm of I/I_0 varies linearly with the apparent density in a range from

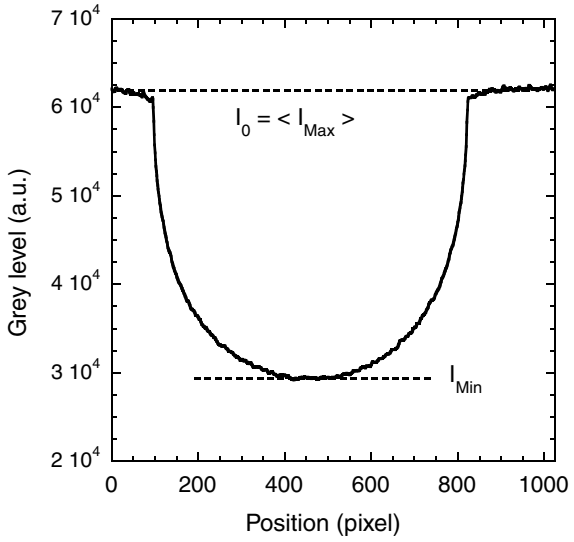

Fig. 3. Variation of the intensity (in grey level) for Tablet n°10 of sample B ($\rho_{app} = 1.275$ g cm^{-3}) versus the pixel position in the projection image along the horizontal direction perpendicular to the cylindrical axis of the compact. (The intensity variation is due to the variation of material width with the position which induces a variation of X-ray absorption. The two horizontal lines represent, respectively, the mean value of the unsaturated intensity I_0 and the lower intensity I_{min} corresponding to the attenuation for $d = d_0 = 11.28$ mm.)

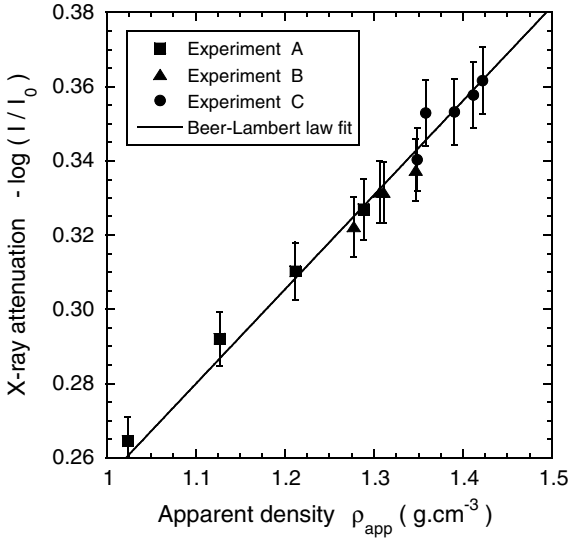

Fig. 4. Variation of the maximum X-ray absorption $-\log(I/I_0)$, as measured from Fig. 3 data, as a function of the apparent density ρ_{app} of cylindrical tablets (g cm^{-3}); $-\log(I/I_0) = 0.2544 \times \rho_{app}$ with $R^2 = 0.9834$. (Each point corresponds to a different tablet and the error bars correspond to an error of 2.5%.)

$\rho_{app} = 1.023$ to 1.420 g cm^{-3} (with a correlation coefficient $R^2 = 0.9834$). This curve results from three different experiments (noted A, B and C). Firstly, from the analysis of this curve (Beer–Lambert theoretical law) where no adjustable parameters are used, we can estimate that the accuracy of the attenuations as function of the apparent density is better than 2.5% (see the error bars corresponding to 2.5% on the Fig. 4). Secondly, no slope differences are visible between the experimental points issued from the three different experiments; one can conclude that the reproducibility of the results is also better than 2.5%. Moreover, the slope of the straight line is proportional to the absorption coefficient. So, this demonstrates that beam hardening effect is negligible in these experimental conditions.

The second method has been used on Tablet n°10 (sample B), which corresponds to an intermediate apparent density (i.e. $\rho_{app} = 1.275$ g cm^{-3}). It consists in measuring the X-ray attenuation $I(x)$ as function of the thickness x, and to check the linearity of $\log(I/I_0)$ vs x. As the tablets are cylindrical, it is easy to calculate the thickness of matter the X-ray beam crosses at a distance r from the centre of the tablet on the projection images. In parallel beam geometry, i.e. in a first step approximation, one gets the thickness x at this point r is related to the cylinder radius R_0 by the equation

$$x = 2\sqrt{R_0^2 - r^2} = 2\sqrt{(d_0/2)^2 - r^2}. \quad (6)$$

Table 2
Variations of density between the central (ρ_{Min}) and the peripheral (ρ_{Max}) zones of the tablets and their associated relative density variations $\Delta\rho/\rho_{Min}$ and $\Delta\rho/\rho_{Max}$

Tablet	ρ_{app} (g cm^{-3})	ρ_{Min} (g cm^{-3})	ρ_{Max} (g cm^{-3})	$(\rho_{Min} + \rho_{Max})/2$ (g cm^{-3})	$\Delta\rho/\rho_{Max}$ (%)	$\Delta\rho/\rho_{Min}$ (%)
1	1.420	1.34	1.49	1.415	10.07	11.19
2	1.410	1.35	1.48	1.415	8.78	9.63
3	1.388	1.34	1.45	1.395	7.59	8.21
4	1.356	1.31	1.42	1.365	7.75	8.40
5	1.347	1.30	1.39	1.345	6.47	6.92
6	1.345	1.29	1.42	1.355	9.15	10.08
7	1.309	1.27	1.38	1.325	7.97	8.66
8	1.305	1.26	1.37	1.315	8.03	8.73
9	1.287	1.23	1.35	1.290	8.89	9.76
10	1.275	1.23	1.33	1.280	7.52	8.13
11	1.210	1.18	1.28	1.230	7.81	8.47
12	1.125	1.09	1.17	1.130	6.84	7.34
13	1.023	0.98	1.04	1.010	5.77	6.12

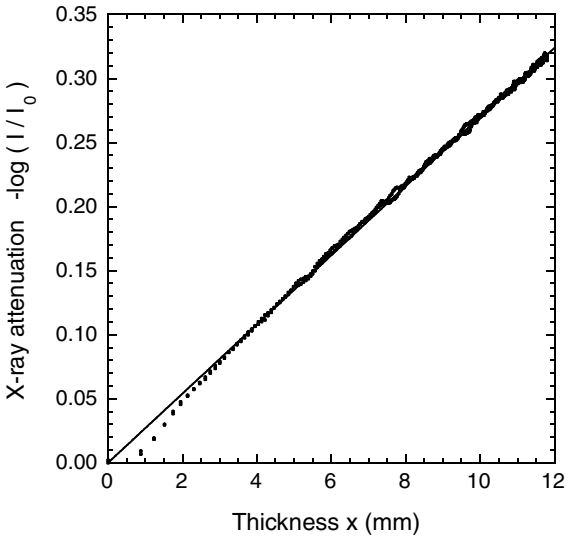

Fig. 5. Relationship between X-ray attenuation $-\log(I/I_0)$ and the thickness x of material crossed by X-ray in the case of a same tablet (i.e. n°10) with an apparent density $\rho_{app} = 1.275\ g\ cm^{-3}$; $-\log(I/I_0) = 0.0270\ x$ with $R^2 = 0.9988$.

The results are represented in Fig. 5. Due to the cylindrical symmetry of the tablet, two measurements of the X-ray-attenuation can be performed for each thickness value x, which correspond, respectively, to the right side and the left one of the tablet (r varying between 0 and 5.64 mm). No significant differences are observed on the Fig. 5 between these two measurements. Fig. 5 exhibits a strong linear relationship between the thickness of matter and its X-ray attenuation (the correlation coefficient $R^2 = 0.9988$), except for the lower values of the thickness ($x < 2$ mm) which correspond to the region near the border of the tablet. The difference with the linear behaviour can be explained by the conical geometry that perturbs the relation between the thickness x and the distance r from the centre defined in Eq. (3) is an approximation which overestimates the thickness near the border.

These two results, summed up in Figs. 4 and 5, show that no beam hardening effect was present on the projection images under our experimental conditions on these tablets. In other words, with our experimental conditions, the Beer–Lambert law is always verified [10] and no mathematical correction has to be used during the reconstruction process of the cross-sectional images. So, the first requirements for quantitative measurements of the apparent density repartition are established.

4.2. Colour-scale calibration on the cross-sectional images

For each sample, after reconstruction, we obtain a set of 950 cross-sectional images, 1024×1024 pixels and 256 grey levels (GL). The second step for quantitative measurements concerns the relationship between the grey level and the apparent density. Depending on its density, for each tablet, the number of cross-sectional images is proportional to the tablet height, so to the inverse of the apparent density; the number of cross-sectional images varies between 164 and 227 for the highest and lowest density, respectively. In order to obtain quantitative measurements of the apparent density from the sectional images for the tablets, it is necessary to correlate the grey level values of the voxels to the apparent density of the tablets.

For this purpose, the average grey value was measured for each tablet on a set of 101 cross-sectional images located in the central zone of the compact, and the measurement was achieved inside a circular region of interest (ROI) of 11 mm diameter corresponding approximately to the tablet dimension (the ROI corresponds to the drawing with black line on Fig. 6b). This statistical analysis was done on the same number of cross-sectional images (101) for each tablet to obtain a set of results which can be compared to each other. The reference value of the mean apparent density used for the calibration was a macroscopic measure obtained from the weight and the entire volume of each tablet. So, this reference value must be compared to a statistical analysis done on a very large number of voxels. With our experimental conditions, the analysis results from 39×10^6 voxels. Due to the spatial resolution 15.63 μm, each voxel corresponds to a cube the volume of which is $(15.63\ \mu m)^3 = 3818\ \mu m^3$. So, the mean grey value results from averaging over 39×10^6 voxels $= 149\ mm^3$ about and has been determined for each density. With this procedure, we are able to compare the different macroscopic measures of the density to the mean grey value calculated on the ROI and finally obtain the calibration relation. The evolution of the mean apparent density ρ_{app} as function of the mean grey level (GL) has been determined from the set of three different experiments. This plot varies linearly as expected (see Fig. 7). According to the error bars (corresponding to an relative error of 2%), we estimate the accuracy and the reproducibility of the results on large enough samples to be better than 2%. For information, $\rho_{app} = -0.0079 \times (GL) + 2.5357$ and the linear correlation between the grey level values and the apparent density is excellent since it corresponds to a correlation coefficient $R^2 = 0.9922$.

At this stage it is worth discussing the accuracy of the experiment. In fact the 2% accuracy which has been determined experimentally in the last paragraph cannot be the result of the intensity fluctuations at the voxel scale, because the number of voxels (39×10^6) it uses is too large, which would result in a fluctuation amplitude of 6 from voxel to voxel. So this accuracy shall result from local density fluctuations. Hence it is worth to study the map of density variation in a tablet. This is done in the next subsection.

4.3. Density maps inside the cylindrical tablets

Image reconstruction leads to a series of cross-section with a distribution of grey intensity (see Fig. 6b). However, fluctuations of voxel intensity from voxel to voxel are too large to allow a direct analysis of the density variations

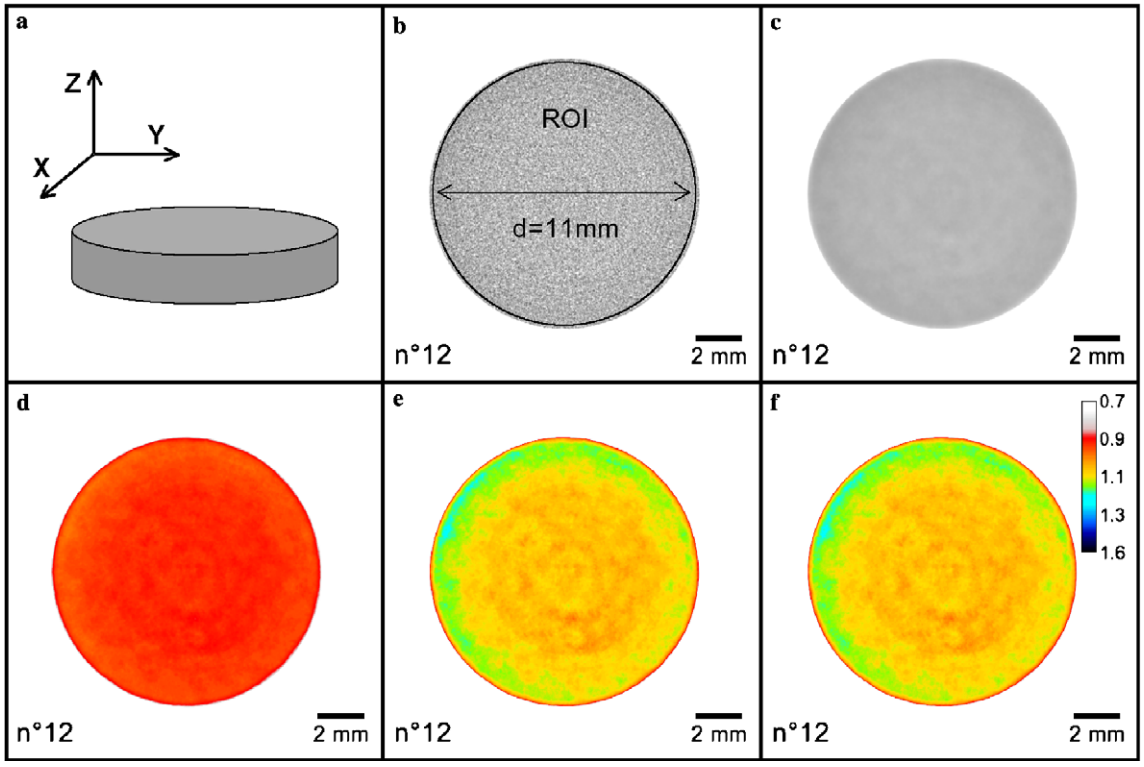

Fig. 6. Different steps of the image processing: (a) coordinate system used for labelling the cross-section planes; (b) example of initial grey-scale cross-section images obtained after reconstruction (Tablet n°12) with the drawing black line corresponding to a circular region of interest (ROI) selected to perform the density calibration (concentric circles correspond to the residue of some ring artefact); (c) median filter effect to reduce the noise of the image; (d) colour LUT; (e) normalization to improve the contrast, see text; (f) final result with the density calibration bar.

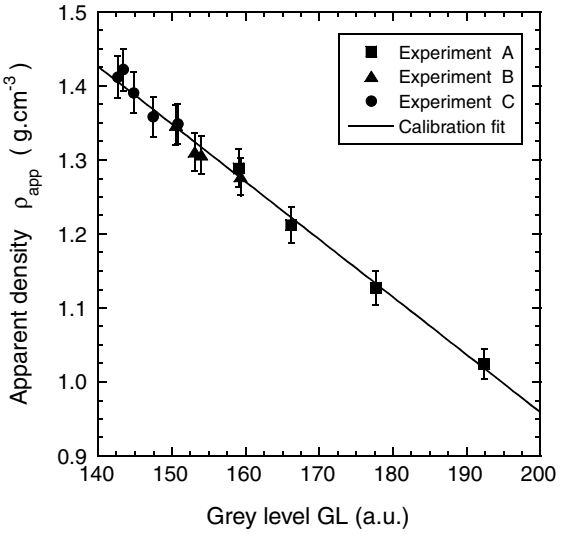

Fig. 7. Grey-scale calibration plot: mean tablet density (ρ_{app}) as a function of the mean grey-scale (GL) obtained after averaging over a volume of the tablet ($\rho_{app} = -0.0079 \times (GL) + 2.5357$; $R^2 = 0.9922$. The error bars correspond to an error of 2%).

in between two different voxel positions since the variations of the mean voxel intensity due to change of density are too weak compared to the fluctuations' amplitude. So the density analysis requires first to improve the quality of the images by a filtering process which avoids rapid variations in space; so a median filter (with a radius of $N_R = 20$ pixels) was applied firstly to reduce the noise of the image (see Fig. 6c). We verified that the median filter treatment did not modify the mean value of the grey level of the cross-section. In fact if $\Delta I/I$ is the local fluctuation, one expects the filtering reduces the noise according to the central limit theorem, as: $\delta I/I = \Delta I/(2N_R I)$.

In a second step, the initial grey scale (8 bit, 256 levels) was changed by an appropriate colour LUT (8 bit, Look-UP Table), as it can be seen in Fig. 6d. Thirdly, a normalization technique (or contrast stretching) was used to increase the contrast of the image: the extreme levels of the pixel values (i.e. p_{min} and p_{max} levels, here $p_{min} = 124$ and $p_{max} = 231$) were extracted from the histogram of the pixel value distribution (considering all the tablets), for each pixel p_i, the new level p_i^{new} was then recalculated using the following formula (see Fig. 6e)

$$p_i^{new} = \frac{p_i - p_{min}}{p_{max} - p_{min}} \times 255. \quad (7)$$

Finally, a calibration bar which relates the colour scale to the apparent density is added to the image to allow simple understanding; it uses the calibration described in the previous paragraph (see Fig. 6f). From this set of images, it is then possible to examine the density distribution in each tablet and to study the dependence of the density distribution upon the mean density of the tablet. One can use

also a statistical treatment to characterize the long range variation of the density inside a tablet itself, introducing a mean square variation as an indicator of the density fluctuations/variations as function of the compaction pressures and in different directions. The different X,Y,Z directions used in this study are defined in Fig. 6a.

5. Discussion

In the present paper, X-ray microtomography has been proved to be a quantitative method to measure the density distribution in pharmaceutical tablets. For instance, a horizontal (X–Y) cross-section and a vertical cross-section (Y–Z) are reported in Figs. 8 and 9 for all studied tablets. Each (X–Y) cross-section corresponds to a cut at mid-height of the compact, with a cut thickness of 15.63 μm. The (Y–Z) cross-sections are obtained from the density variation across the tablet diameter of the (X–Y) cross-sections. To allow an easier discussion of the quantitative results, the same scale of colour is used for all these images in density (g cm^{-3}). From these series of images one can conclude few results.

One observes firstly that all tablets exhibit a cylindrical symmetry for the density distribution as observed from the mid cuts' (X–Y) cross-section reported in Fig. 8. One can see an evolution of this density with the distance to the tablet axis, which is a consequence of the compaction process with cylindrical die. Indeed, for all samples, density looks not homogeneous in the (X–Y) cross-section, with a high density area observed always in the periphery of tablet, i.e. those regions which were in contact with the die walls during the manufacturing process. This result is also confirmed by the observation of (Y–Z) cross-sections (see Fig. 9) which present clearly two zones: the first one, a circular region localized in the middle of the tablet and a second one denser corresponding to a ring close to the die walls. So, for each image, the density of a small ring area can be measured as a function of its distance from the tablet centre: it is a radial density profile. In Fig. 10, we report these radial density profiles for 2 different tablets corresponding to large density (Tablet n°1) and lowest density (Tablet n°13), respectively. For example, in the case of Tablet n°1 ($\rho_{app} = 1.42$ g cm^{-3}), the density in the middle ρ_{Min} is about 1.3 g cm^{-3} whereas the surface density is 1.5 g cm^{-3}. Assuming that the density variation between the two regions is $\Delta\rho = \rho_{Max} - \rho_{Min}$ where ρ_{Max} is the largest density (peripheral ring) and ρ_{Min} is the smaller density (circular centred region), the relative density variation defined as $\Delta\rho/\rho_{Min}$ varies continuously between 11.2% and 6.1% when the mean apparent density ρ_{app} ranges from 1.420 g cm^{-3} (Tablet n°1) to 1.023 g cm^{-3} (Tablet n°13) (see Table 2). This heterogeneity of density observed between the centre and the periphery of these cylindrical tablets is significant since its variation is larger than the accuracy on the density measurements in our experimental conditions (about 3%). These profiles show that heterogeneity (i.e. $\Delta\rho/\rho_{Min}$) becomes more important as the mean apparent density ρ_{app} increases (i.e. as the applied compaction pressure is higher), which means in other words that the compaction process generates an heterogeneous distribution of density, and the larger the compaction pressure the larger the effect.

The consequence of a variation of the tablet density is that it is necessary to differentiate the surface mechanical properties (indentation hardness for example) and the volume mechanical properties (Young's modulus, tensile strength,...). Contrary to what is generally made [4,15], these properties could not be explained by the same way. Fig. 11 shows the results of the Brinell hardness measurement performed on tablets obtained under the same compaction conditions than the tablets of Table 1. The microindentation test and the Brinell hardness measurement were described in detail in reference [12]. The mechanical properties of compacted samples (in this case, Brinell hardness) are commonly linked to the mean compact porosity using an empiric exponential relationship [16] (Fig. 12, full circle symbols). The extrapolated value at a zero porosity is generally used in order to get information on the continuous solid. In the case of the Vivapur 12® compacts, if the mean porosity is considered, the obtained extrapolated value is slightly higher ($H_b = 78.06 \times e^{-6.3256 \times \varepsilon mean}$, $R^2 = 0.9681$; full circle symbols in Fig. 11) than one and half the extrapolated value obtained with the surface porosities ($H_b = 57.279 \times e^{-5.7525 \times \varepsilon surface}$, $R^2 = 0.9753$; full triangle symbols in Fig. 11). In the case of the surface properties, the error in the extrapolated value may be important. Therefore, in reference to the heterogeneity of density (and then, to the heterogeneity of porosity) observed by the X-ray μCT technique between the surface and the centre of the compact (see Fig. 12), it may be more suitable to link the Brinell hardness results to the porosity measured in surface using X-ray tomography technique (Fig. 12, full triangle symbols).

According to Fig. 10, the thickness of the denser peripheral ring is in a range of 0.6–1.0 mm depending on the tablet's density. The thickness seems to decrease with the increase of compaction pressures. This ring is important to consider in other cases such as the study of the tablet friability. In fact, the capacity of a tablet to resist to the shocks depends on the density of this area. More, it could lead to picking in particular within the "closed" numbers and letters that form "islands". If the thickness of the logos is almost the same as the denser area, the logos can behave like a cutter, and sticking can occur.

Figs. 10 and 13 report the density distribution (in (X–Y) cross-sections) in three different cuts and the evolution of the radial density profile for the samples n°1 and 13 corresponding to three different positions along Z axis (top, middle and bottom of the tablet). The two extreme cuts (top–bottom) are located at 100 μm below or above the free surfaces. Concerning the Tablet n°1, the density in periphery does not vary along the Z axis, but, the density in the middle is slightly higher near the bottom of the compact. In Figs. 13(e)–(g) and for the Tablet n°13, the three images

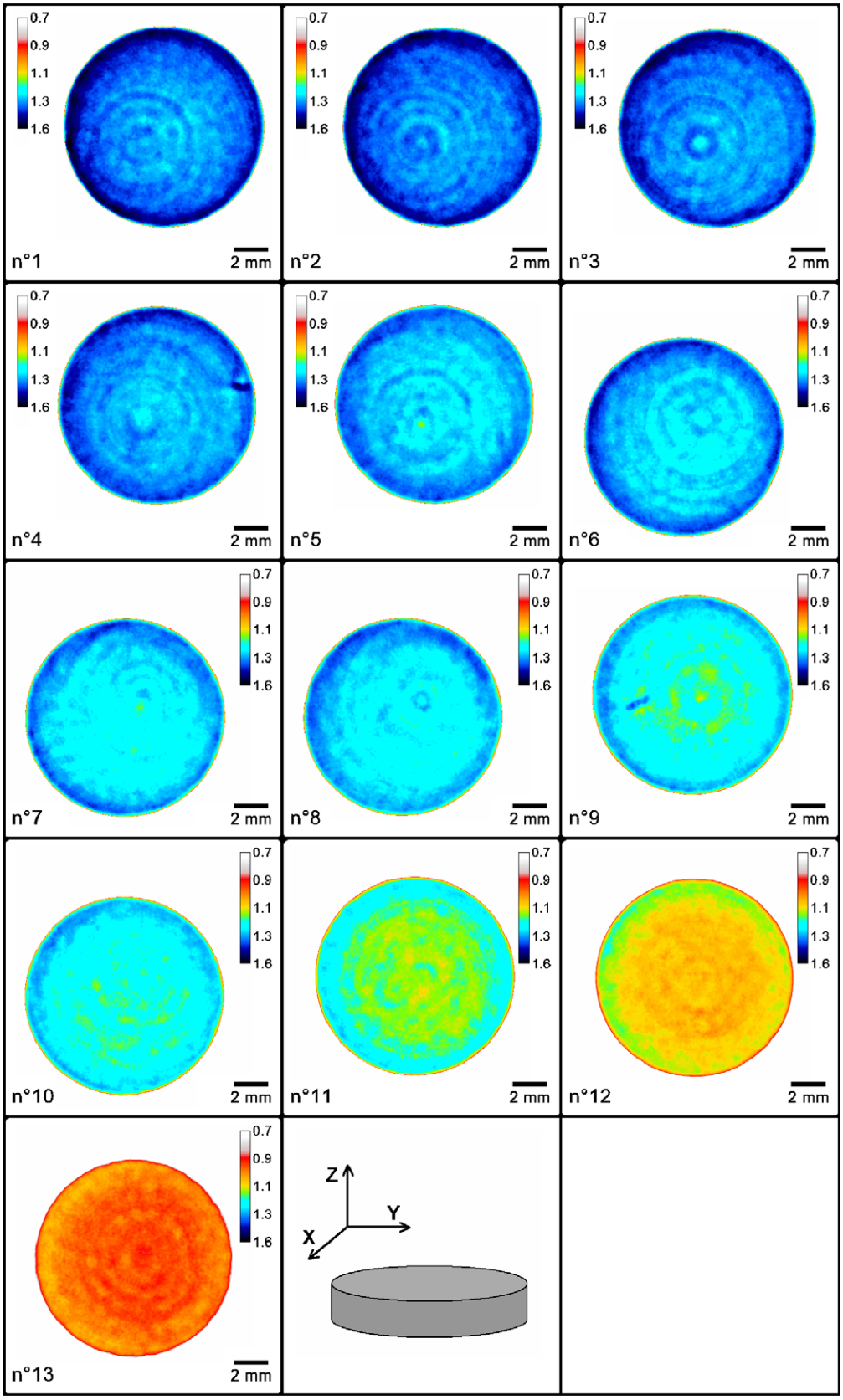

Fig. 8. Density distribution in the horizontal X–Y cross-sections obtained from reconstructed images at mid-height of the tablets; the number of the tablet refers to Table 1.

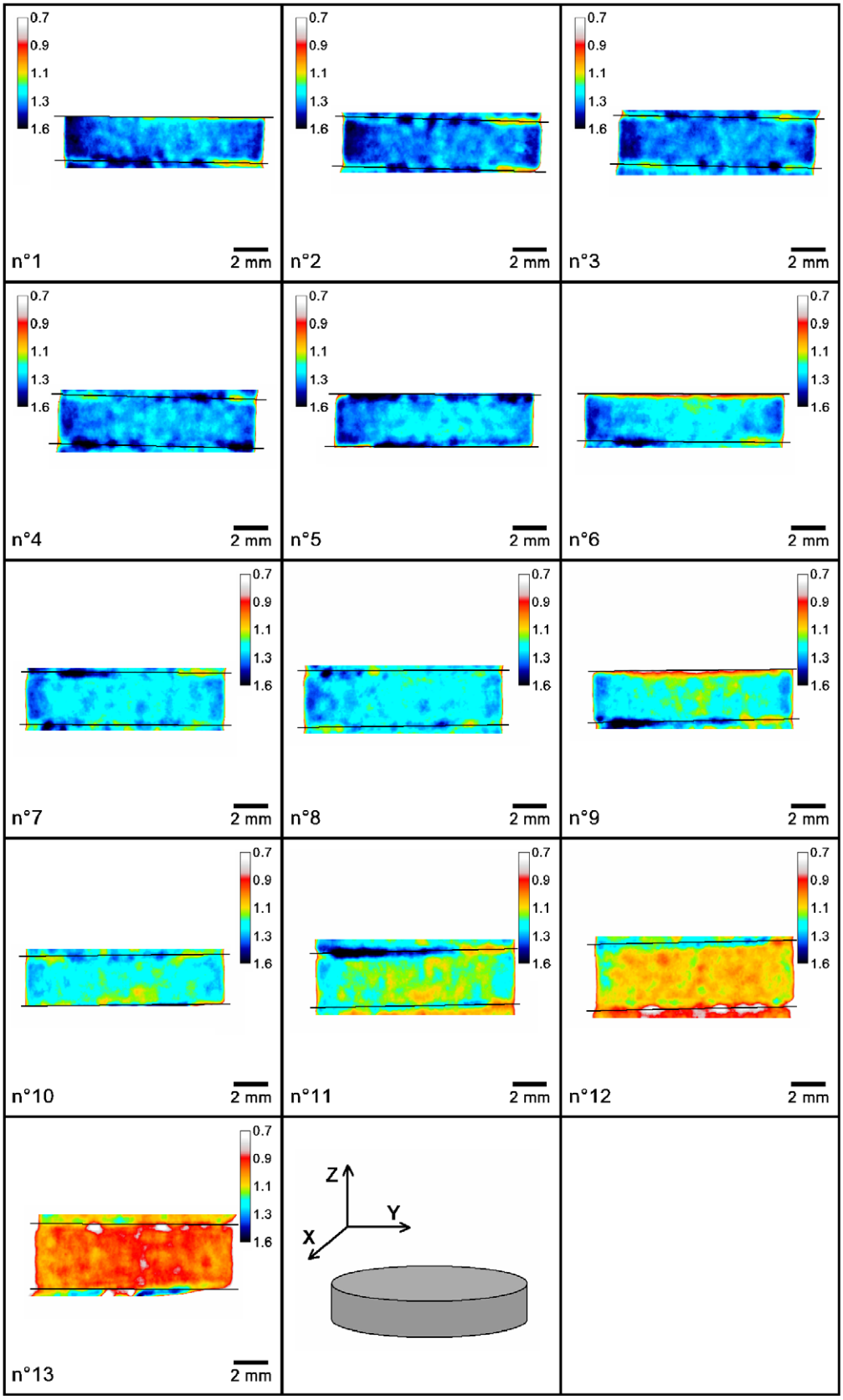

Fig. 9. Density distribution in the vertical *Y–Z* cross-sections obtained from reconstructed images; the number of the tablet refers to Table 1 (the black straight lines correspond about to the edge of the different tablets).

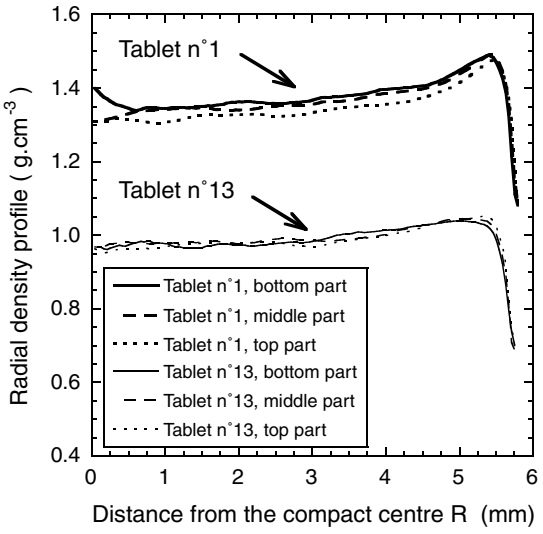

Fig. 10. Radial density profiles obtained in horizontal X–Y cuts for the two extreme density tablets (Tablet n°1, $\rho_{app} = 1.420\ g\ cm^{-3}$ and Tablet n°13, $\rho_{app} = 1.023\ g\ cm^{-3}$) obtained from reconstructed images (these cross-sections correspond to cuts located at mid-height of the compacts and at 100 μm below and above the free surfaces).

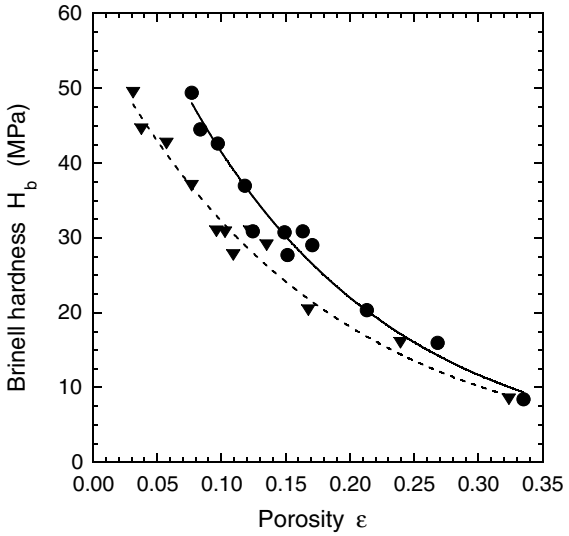

Fig. 11. Exponential relationship between porosity (mean porosity, ε_{mean}, ● and surface porosity, $\varepsilon_{surface}$, ▼) and Brinell hardness (H_b) for Vivapur 12® compacts.

look more similar, pointing out that on average, the density distribution along the Z axis is rather uniform (homogeneous). This is also confirmed by the variation of the radial density profile in Fig. 10. In this graph, the three radial density profiles obtained in the case of Tablet n°13 are superimposed. For a same tablet, it can be also observed that on average, the density variations are more important between the middle and the compact periphery than between the top and the bottom part.

Figs. 13(d) and (h) show the density distribution in the vertical Y–Z cross-sections which is commonly used in numerical simulations [17]. In these cross-sections,

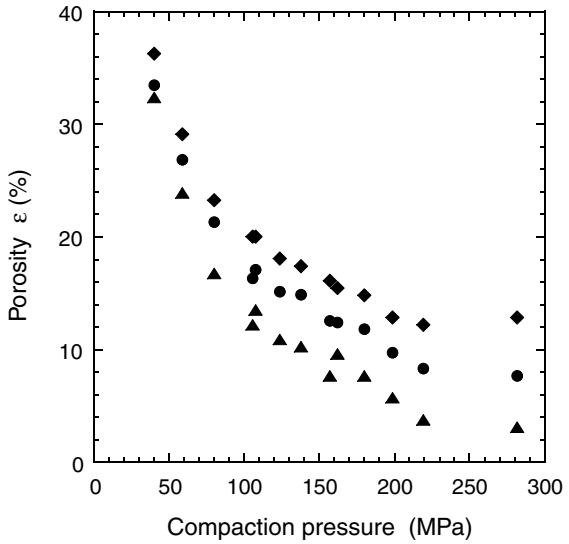

Fig. 12. Comparison between the minimum porosity (▲) and the maximum porosity (♦) determined by X-ray microtomography and the mean calculated porosity (●) for various compaction pressures.

there are locally some heterogeneities in density. A high density region is observed near the right and left parts of the considered Y–Z plane. A region of lower density in the middle bottom part of the compact and an area of higher density in the middle of the compact are also observed. The area of higher density on the middle of the compact is about the same density level than near the right and left parts. These local areas of heterogeneity are blended into a region of intermediate density. These results are qualitatively in good accordance with previous experimental works [4,10] and with numerical modelling [17,18].

6. Conclusion

X-ray tomography was applied successfully to the study of the density of pharmaceutical cylindrical tablets. First, this study had shown the importance of checking the validity of the Beer–Lambert law. In the case of cylindrical compact of microcrystalline cellulose with our experimental conditions, the law is valid and the beam-hardening correction is not necessary. The perfecting of the technique was also explained and density maps were obtained for tablets of various porosities. In all cases, an important heterogeneity in density was observed in the X–Y cross-sections, with higher densities in peripheral region and lower densities in the middle compared to the total mean apparent density. More, the results obtained in the Z–Y cross-sections are in accordance with previous results of the literature.

This technique that has the advantage to be nondestructive could be helpful to understand the compaction process. Moreover, the results of this study underlined that in the case of pharmaceutical cylindrical tablets, it is important to differentiate the mechanical properties

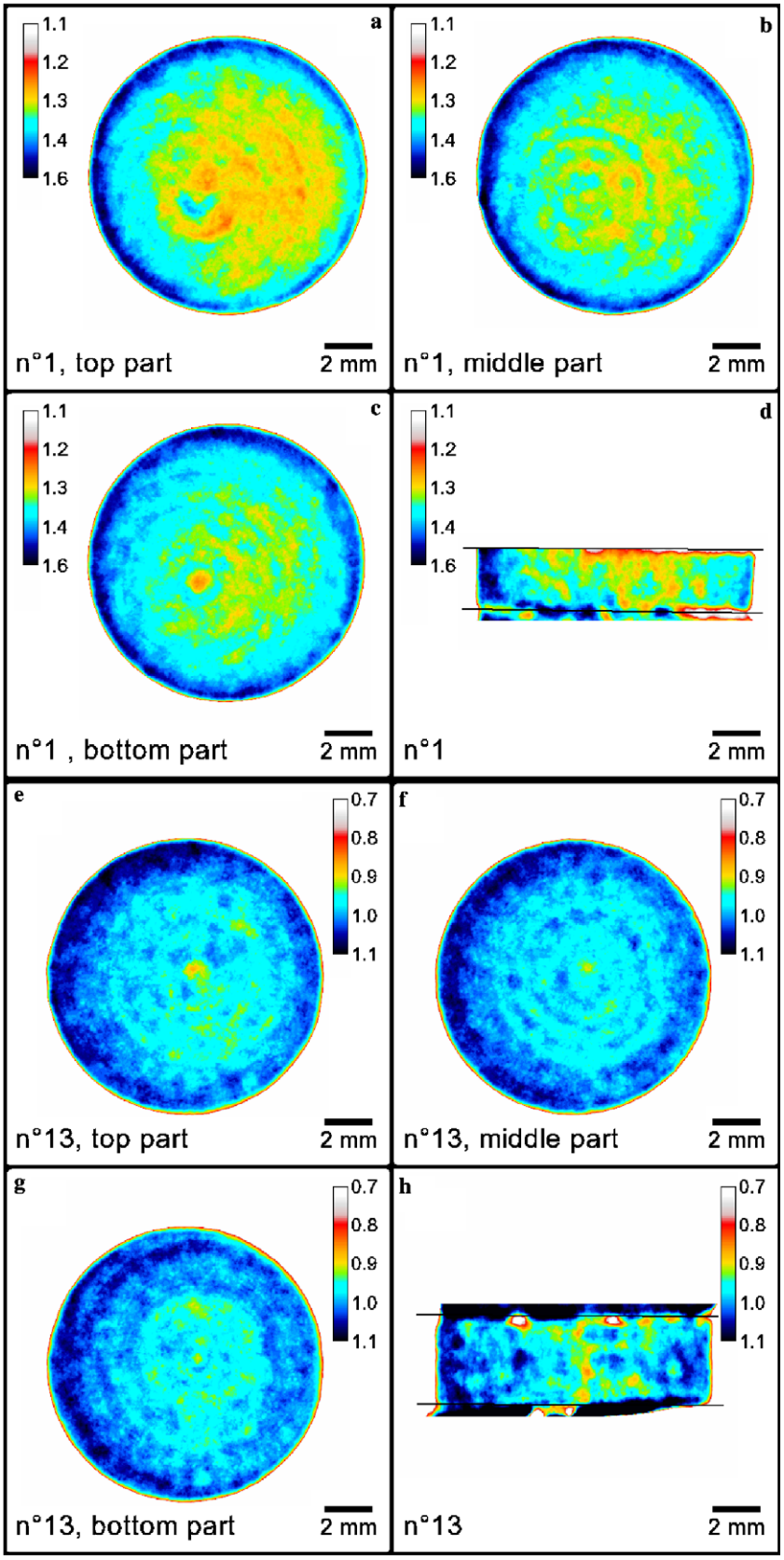

Fig. 13. Density distributions obtained from 2D reconstructed images corresponding to a cut of 15.63 μm thickness of Tablets n°1 (a–d) and n°13 (e–g); (a–c and e–g) horizontal X–Y cross-sections' density distribution located at different position along the Oz compression axis; (d and h) vertical (Y–Z) cross-sections.

representative of the total volume tablet and the mechanical properties that only characterize the tablet surface.

Acknowledgements

The High-resolution micro-CT system SkyScan-1072 XRCT® and the workstations were purchased thanks to grants from the Région Centre (France).

References

[1] D. Train, An investigation into the compaction of powders, J. Pharm. Pharmacol. 8 (1956) 745–761.
[2] G. Nebgen, D. Gross, V. Lehmann, F. Muller, H-NMR microscopy of tablets, J. Pharm. Sci. 84 (1995) 283–291.
[3] H.M. Macleod, K. Marshall, The determination of density distributions in ceramic compacts using autoradiography, Powder Technol. 16 (1977) 107–122.
[4] I.C. Sinka, J.C. Cunningham, A. Zavaliangos, The effect of wall friction in the compaction of pharmaceutical tablets with curved faces: a validation study of the Drucker-Prager Cap model, Powder Technol. 133 (2003) 33–43.
[5] L. Farber, G. Tardos, J.N. Michaels, Use of X-ray tomography to study the porosity and morphology of granules, Powder Technol. 132 (2003) 57–63.
[6] I.C. Sinka, S.F. Burch, J.H. Tweed, J.C. Cunningham, Measurement of density variations in tablets using X-ray computed tomography, Int. J. Pharm. 271 (2004) 215–224.
[7] L. Salvo, P. Cloetens, E. Maire, S. Zabler, J.J. Blandin, J.Y. Buffière, W. Ludwig, E. Boller, D. Bellet, C. Josserond, X-ray micro-tomography an attractive characterisation technique in materials science, Nucl. Instrum. Methods B 200 (2003) 273–286.
[8] A.C. Kak, Computerized tomography with X-ray, emission and ultrasound sources, Proc. IEEE 9 (1979) 1245–1272.
[9] D.H. Phillips, J.J. Lannutti, X-ray computed tomography for the testing and evaluation of ceramic process, Am. Ceram. Soc. Bull. 72 (1993) 69–75.
[10] D.H. Phillips, J.J. Lannutti, Measuring physical density with X-ray computed tomography, NDT&E Int. 30 (1997) 339–350.
[11] V. Busignies, P. Tchoreloff, B. Leclerc, M. Besnard, G. Couarraze, Compaction of crystallographic forms of pharmaceutical granular lactoses. I. Compressibility, Eur. J. Pharm. Biopharm. 58 (2004) 569–576.
[12] V. Busignies, P. Tchoreloff, B. Leclerc, C. Hersen, G. Keller, G. Couarraze, Compaction of crystallographic forms of pharmaceutical granular lactoses. II. Compacts mechanical properties, Eur. J. Pharm. Biopharm. 58 (2004) 577–586.
[13] L.A. Feldkamp, L.C. Davis, J.W. Kress, Practical cone-beam algorithm, J. Opt. Soc. Am. 1 (1984) 612–619.
[14] W.S. Rasband, ImageJ, U.S. National Institutes of Health, Bethesda, Maryland, USA (1997–2005). http://rsb.info.nih.gov/ij/.
[15] W. Jetzer, H. Leuenberger, H. Sucker, The compressibility and compactibility of pharmaceutical powders, Pharm. Technol. (1983) 33–39.
[16] E. Ryshkewitch, Compression strength of porous sintered alumina and zirconia, J. Am. Ceram. Soc. 36 (1953) 65–68.
[17] I. Aydin, B.J. Briscoe, K.Y. Sanhtürk, The internal form of compacted ceramic components: a comparison of a finite element modelling with experiment, Powder Technol. 89 (1996) 239–254.
[18] A. Michrafy, D. Ringenbacher, P. Tchoreloff, Modelling the compaction behaviour of powders: application to pharmaceutical powders, Powder Technol. 127 (2002) 257–266.